

Automated Segmentation of the Melanocytes in Skin Histopathological Images

Cheng Lu, Muhammad Mahmood, Naresh Jha, and Mrinal Mandal, *Senior Member, IEEE*

Abstract—In the diagnosis of skin melanoma by analyzing histopathological images, the detection of the melanocytes in the epidermis area is an important step. However, the detection of melanocytes in the epidermis area is difficult because other keratinocytes that are very similar to the melanocytes are also present. This paper proposes a novel computer-aided technique for segmentation of the melanocytes in the skin histopathological images. In order to reduce the local intensity variant, a mean-shift algorithm is applied for the initial segmentation of the image. A local region recursive segmentation algorithm is then proposed to filter out the candidate nuclei regions based on the domain prior knowledge. To distinguish the melanocytes from other keratinocytes in the epidermis area, a novel descriptor, named local double ellipse descriptor (LDED), is proposed to measure the local features of the candidate regions. The LDED uses two parameters: region ellipticity and local pattern characteristics to distinguish the melanocytes from the candidate nuclei regions. Experimental results on 28 different histopathological images of skin tissue with different zooming factors show that the proposed technique provides a superior performance.

Index Terms—Histopathological image analysis, image segmentation, local descriptor, object detection, pattern recognition.

I. INTRODUCTION

SKIN cancer is the most frequent and malignant type of cancer [1], and melanoma is the most aggressive type among skin cancers. It has been stated that approximately 70 000 people are diagnosed with melanoma skin cancer, and about 9 000 people die from it in the U.S. every year [2]. The early detection of malignant melanoma is crucial to lower the mortality from this cancer. Approaches to melanoma diagnosis have dynamically evolved during the last 25 years [3]. Although there are many new emerging techniques, e.g., confocal microscopy [4], which can provide initial diagnosis, pathological examination remains the gold standard for the diagnosis as the histopathology slides provide a cellular level view of the disease [5].

Manuscript received September 6, 2011; revised January 16, 2012 and April 5, 2012; accepted May 2, 2012. Date of publication May 16, 2012; date of current version March 8, 2013.

C. Lu and M. Mandal are with the Department of Electrical and Computer Engineering, University of Alberta, Edmonton, AB T6G 2V4, Canada (e-mail: lcheng4@ualberta.ca; mandal@ece.ualberta.ca).

M. Mahmood is with the Department of Laboratory Medicine and Pathology, University of Alberta, Edmonton, AB T6G 2B7, Canada (e-mail: nausherwan.mahmood@albertahealthservices.ca).

N. Jha is with the Department of Oncology, Cross Cancer Institute, University of Alberta, Edmonton, AB T6G 1Z2 (e-mail: naresh.jha@albertahealthservices.ca).

Color versions of one or more of the figures in this paper are available online at <http://ieeexplore.ieee.org>.

Digital Object Identifier 10.1109/TITB.2012.2199595

Traditionally, the histopathology slides are examined under a microscope by pathologists. The diagnosis is then based on the personal experience of pathologists. However, this judgement is subjective and often leads to intra-observer and inter-observer variability [6]. To address this problem, automated computational tool which can provide reliable and reproducible objective results for quantitative analysis are desirable.

In melanoma diagnosis, the segmentation and detection of the melanocytes in the epidermis area is an important step before the diagnosis is made. If the melanocytes can be found correctly, architectural and cellular features (e.g., size, distribution, location) can be used to grade or determine the malignancy of the skin tissue.

The digitized histopathological images we used in this study are stained with haematoxylin and eosin (H&E). Three examples of the skin epidermis image are shown in Fig. 1. The cell nuclei are observed as dark blue, whereas the intracellular material and cytoplasm are observed as bright pink. It is also noted that there exist color variations in interimages and intrimages due to nonuniform absorption of the stain, and different handling procedure or other factors, e.g., stains fading. In addition, the high similarity between the melanocytes and other cytological components make it difficult to perform consistent quantitative analysis.

Several works have been conducted on the segmentation or detection of various biological components in a histopathological image using image-processing techniques such as thresholding [7]–[9] and watershed [10]. Gurcan *et al.* [7] proposed a hysteresis threshold-based technique for the nuclei segmentation in neuroblastoma image. The technique first employs morphological operations to reduce the background signal. The hysteresis thresholding was then used to perform the segmentation. Petushi *et al.* [8] proposed to use adaptive threshold-based technique for the nuclei segmentation in the breast cancer image. With the assumption that the nuclei are bright objects in a relatively uniform dark background, Chen *et al.* [11] proposed the use of global threshold and watershed technique to segment the cancer cell nuclei in time-lapse microscopy. These threshold-based techniques typically fail when considerable intensity variations are present in the images. Nattkemper *et al.* [12] proposed a fluorescent lymphocytes detection technique using trained artificial neural networks. By incorporating the color, texture, and shape information present in an image, Naik *et al.* [13] proposed to segment the nuclei using the Bayesian classifier. Sertel *et al.* [14] computed the probability map of karyorrhexis cells based on the estimated likelihood function, and the cell nuclei are then segmented using thresholding. Although these techniques have been reported to provide good performance, the performance is

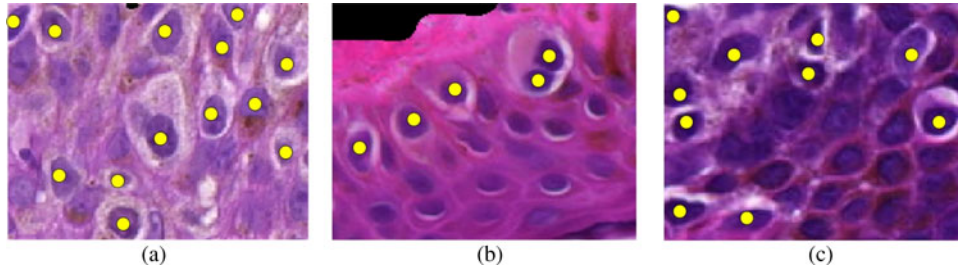


Fig. 1. Melanocytes of epidermis area in different skin tissues. Interimage and intrainage variations are observed in terms of the color. These images are obtained from the digitized skin slides. The yellow seed points indicate the location of melanocytes, whereas other nuclei are keratinocytes.

sensitive to the training samples. The histopathological images used in our paper contain interimage and intrainage intensity variations due to the staining imperfection. Also, because of the natural biological features of the skin epidermis, the foreground and the background objects have similar intensity values. Therefore, many of the aforementioned techniques seem unsuitable for our scenario.

In the melanocytes segmentation, the main difficulty is how to differentiate the melanocytes and other keratinocytes in the skin epidermis area. These two kinds of cells have similar intensity and nuclei size. A similar problem has been addressed by Basavanthally *et al.* [15] in breast cancer diagnosis, where the lymphocyte nuclei are differentiated from the cancer cell nuclei in H&E stained histopathological images. In their work, the two kinds of cells (cancer cell and lymphocytes) are differentiated based on the domain knowledge such as the nuclei size, intensity of the nuclei, and spatial proximity. However, in skin histopathological images, the size of melanocytes are very similar to that of other keratinocytes. Due to the interimage and intrainage variations, the intensity value of the melanocytes and other keratinocytes are very close to each other. Therefore, the domain knowledge used in breast cancer detection [15] will not work well in the case of melanocytes detection.

There is another closely related work in the literature, where all the keratinocytes nuclei are segmented in the skin epidermis area [16]. In this work, a threshold is calculated based on the assumption that cell nuclei covers approximately the darkest 20% of the pixel in the image. The pixels whose values are less than the threshold are labeled as nuclei regions. Morphological operations are then used to refine the segmented result. However, this global threshold based technique only works under the assumption that there is no intensity variations in the image, and usually generates under-segmentation results (many of the nuclei are grouped together). Also, there is no attempt to differentiate the melanocytes and other keratinocytes.

Template-matching (TM) technique is a popular technique in computer vision for pattern detection. Naik *et al.* [13] have used four binary elliptical templates with different major and minor axes to detect the nuclei in breast-cancer histopathological images. It is observed in Fig. 1 that the melanocytes typically have low-intensity values, while its spatial surrounding space has brighter intensity values. It may be possible to detect the melanocytes using TM technique with templates that have round darker heart encompassed by a brighter ring. However, several

difficulties need to be addressed. First, the size of the template is hard to decide due to the size variations of the melanocytes even under the same magnification level. In the case of skin cancer, the melanocytes are larger than that in the case of normal skin or nevus skin. Second, the intensity level of the template is hard to determine. Therefore, it is difficult to decide a “good” template to match the melanocyte patterns.

In order to address the earlier mentioned problems, we propose a novel technique to segment and detect the melanocytes in the skin epidermis area in this paper. Unlike the existing techniques which usually assume relatively uniform background, the proposed technique considers the interimage and intrainage variations due to the staining imperfection. Also, the proposed technique can provide good detection performance on histopathological images, where the background is complex and has similar appearance with the foreground (i.e., the melanocytes). Furthermore, the proposed technique models the natural biological features, i.e., the shape and the distribution of intensity, as the parameters which make the technique robust. To our best knowledge, this is the first automated technique for joint segmentation and detection of the melanocytes in histopathological image of skin tissue. This technique operates on reliable quantitative measures and provides objective and reproducible information complementary to that of a pathologist. Such quantitative analysis of melanocytes is important for clinical applications as well as for research purpose.

The organization of this paper is as follows. The proposed technique is described in Section II, followed by the performance evaluations in Section III. The conclusions are presented in Section IV.

II. THE PROPOSED TECHNIQUE

In this section, we present the proposed technique which is primarily based on the local feature space analysis. The schematic of the proposed technique is shown in Fig. 2 which consists of three main steps. In the first step, we segment the candidate nuclei regions in the epidermis area using the mean-shift segmentation [17]. The mean-shift segmentation clusters the pixels into local regions based on the color similarity and spatial closeness. In the second step, a local region recursive segmentation (LRRS) algorithm is proposed to detect the candidate nuclei regions from the mean-shift segmented image. In the last step, a novel descriptor, named local double ellipse descriptor

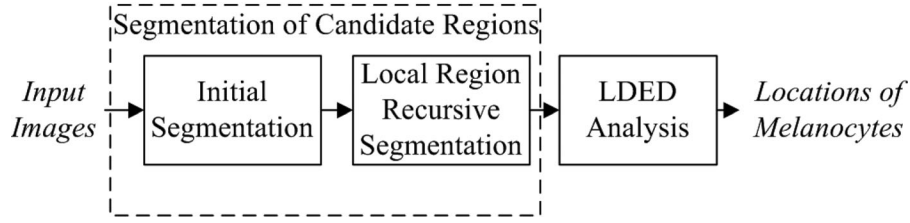


Fig. 2. The schematic of the proposed technique.

(LDED), is proposed to perform the quantitative analysis. This descriptor builds two ellipsoid models based on the segmented candidate regions. The LDED then measures the local feature information using two well-defined parameters which incorporate the biological pattern of the melanocytes. The location of the melanocytes can then be identified by the LDED. The steps in the proposed technique are now presented in details in the following.

A. Initial Segmentation

Due to the staining imperfection and variations, the appearance of individual cytological components is not homogeneous, and have complex texture surface. In order to reduce such variations, initial segmentation is required to decompose the original image into homogeneous biological components. Several existing robust low-level segmentation methods, such as level set [18] and mean shift [17] can be used for this purpose.

In this paper, the mean-shift segmentation [17] is applied to perform the initial segmentation because of its ability to preserve the local boundaries. The mean-shift segmentation first estimates the key features of interest or modes (i.e., stationary points of the density of image intensity) of the underlying density function of the image intensity. It then clusters the pixels into different regions based on the corresponding modes.

Given an image, let n be the total number of pixels in the image. Let the pixel feature vector set in d -dimensional Euclidean space \mathbf{R}^d for all the pixels in the image be denoted by $X = \mathbf{x}_1, \mathbf{x}_2, \dots, \mathbf{x}_n$. For each feature vector $\mathbf{x}_i \in X$, there is a corresponding mode \mathbf{y}_i . In the beginning, the mode \mathbf{y}_i is initialized with the feature vector value \mathbf{x}_i , i.e., $\mathbf{y}_i^0 = \mathbf{x}_i$. The \mathbf{y}_i^u is then recursively updated, based on the neighborhood characteristics, using the following equation:

$$\mathbf{y}_i^{u+1} = \mathbf{y}_i^u + \mathbf{m}_G(\mathbf{y}_i^u), 1 \leq i \leq n \quad (1)$$

where \mathbf{y}_i^{u+1} is the updated version of \mathbf{y}_i^u . The vector $\mathbf{m}_G(\mathbf{y}_i)$ is called the mean-shift vector and defined as follows:

$$\mathbf{m}_G(\mathbf{y}_i) = \frac{\sum_{j=1}^n \mathbf{x}_j g(\|\frac{\mathbf{y}_i - \mathbf{x}_j}{h}\|^2)}{\sum_{j=1}^n g(\|\frac{\mathbf{y}_i - \mathbf{x}_j}{h}\|^2)} - \mathbf{y}_i \quad (2)$$

where $g(\cdot)$ is the 1-D profile of multidimensional kernel $G(\cdot)$, and h is the kernel bandwidth. In this paper, we chose $g(x) = \exp(-\frac{1}{2}x)$ for $x \geq 0$. The mean-shift vector calculates the difference between the weighted mean and the center of the kernel and it can be shown [17] that it always points toward the direction of maximum increase in the underlying density function. At the

end, each pixel \mathbf{x}_i can find a corresponding mode \mathbf{y}_i which will be used for the segmentation.

In this paper, a 5-D feature space is used. The features used are two spatial coordinates of the 2-D image and three color channels {R,G,B}. The corresponding multivariate kernel is defined as the product of two radially symmetric kernels as follows:

$$K_{h_s, h_c}(\mathbf{x}_i) = \frac{C}{h_s^2 h_c^3} k\left(\left\|\frac{\mathbf{x}_i^s}{h_s}\right\|\right) k\left(\left\|\frac{\mathbf{x}_i^c}{h_c}\right\|\right) \quad (3)$$

where $k(\cdot)$ is the profile of the kernel, \mathbf{x}^s is the spatial component, \mathbf{x}^c is the color component, C is the normalization constant, and h_s and h_c are the kernel bandwidths controlling the size of the kernels for spatial and color component, respectively. Note that the higher value of the kernel bandwidths h_s and h_c correspond to more neighboring data points that are used to estimate the density.

The mean-shift segmentation is then computed as follows [17].

- 1) Run the mean-shift iteration in (1) and store the mode \mathbf{y}_i for each 5-D point \mathbf{x}_i in the feature space.
- 2) Form clusters $\{C_p\}_{p=1 \dots P}$ by grouping the modes \mathbf{y} if the distances between the spatial domains and the distances between the color domains are less than h_s and h_c , respectively.
- 3) Fuse the spatial regions which have less than Q pixels with their nearest regions in spatial domain.

Note that there is a tradeoff between the parameters h_s , h_c , and Q . The higher values of parameters h_s , h_c , and Q correspond to a coarser segmentation, and vice versa. In this paper, we have used the parameter value $h_s = 6$, which means, for each pixel, its spatial neighbors within a circle of radius six pixels are used to estimate the density. We have used the parameter value $h_c = 6$, which means, for each pixel in the 3-D {R, G, B} color space (where each channel has 256 gray levels), its neighbors within a sphere with radius of six voxels are used to estimate the density. We have used the parameter value $Q = 30$ (a region with area less than 30 pixels will be merged with one of its neighbors). Note that since the size of natural nuclei typically falls within a certain size range, this parameter set can provide good performance for the histopathological images captured under $30\times$ magnification. For other magnification, we can adjust the parameters by multiplying the zooming factors accordingly.

Fig. 3 shows an example of the original image and the segmented image obtained using the mean-shift segmentation. It is

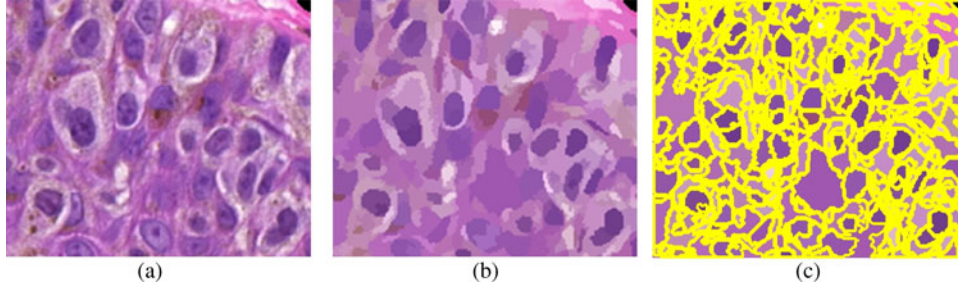


Fig. 3. An example of the mean shift segmentation. (a) Original image. (b) Segmented image by mean-shift segmentation [17]. (c) Boundaries of all the segmented regions.

clear that the local-intensity variation is reduced, while the local object boundary is well preserved.

B. Local Regions Recursive Segmentation

After applying the mean-shift segmentation, the pixels which have intensity similarity and geometric closeness are clustered together. The mean-shift-segmented image consists of many segmented regions which are denoted as $\{R_p\}_{p=1\dots Z}$, where Z is the total number of regions. Fig. 3(c) shows the segmented regions $\{R_p\}_{p=1\dots Z}$, where the boundary for each region is highlighted by a yellow contour. In this paper, the object of interest is the nuclei regions in the epidermis area. Our next step is to segment the candidate nuclei regions based on the mean-shift-segmented regions $\{R_p\}_{p=1\dots Z}$. In this section, we present a split-and-merge-based algorithm, named local region recursive segmentation (LRRS) to segment the nuclei regions. In the proposed LRRS algorithm, two domain-specific knowledge are incorporated: 1) the intensity of the nuclei is lower than that in the cytoplasm; 2) the size of a candidate nuclei region is within a predefined range. The LRRS algorithm has two steps that are detailed in the following.

Step 1: We calculate the mean intensity $\{q_p\}_{p=1\dots Z}$ for each region in $\{R_p\}_{p=1\dots Z}$. We then calculate a global threshold T_g using Otsu's method [19] for the mean intensity set $\{q_p\}_{p=1\dots Z}$, followed by truncation of the region whose mean intensity is greater than T_g . After the truncation, most of the regions representing the cytoplasms are removed. Fig. 4(a) shows an image obtained by applying step 1.

Step 2: The remaining adjacent regions are merged to form the new regions set $\{R'_p\}_{p=1\dots Z'}$. Note that in these merged regions, there are undersegmented regions, i.e., the regions which contain several nuclei or other noisy components, due to the intensity variation in the epidermis. Based on the domain knowledge that the nuclei region should be within an area range, a size prior criterion T_{area} is defined. T_{area} is the upper bound of the candidate nuclei region. For each merged region R'_p , we estimate the number of intensity values v and the area $A(R'_p)$. The local region R'_p which satisfies the following conditions

$$A(R'_p) > T_{area} \quad \text{and} \quad V > 2 \quad (4)$$

will be further split into subregions using the mean value of current region R'_p . For the regions which do not satisfy the earlier mentioned conditions, we assign these regions to the

candidate nuclei regions set $\{N_p\}_{p=1\dots K}$. We repeat this split-and-merge strategy until there is no region satisfying the condition shown in (4). An example of the undersegmented regions is illustrated in Fig. 4(c), where the $A(R'_p) > T_{area}$, and we observe four different values: q_1, q_2, q_3 , and q_4 . The split result corresponding to Fig. 4(c) is illustrated in Fig. 4(d). Note that the regions containing values q_1 and q_4 are removed since $q_4, q_1 > \text{mean}(q_1, q_2, q_3, q_4)$. The final version of the nuclei region set $\{N_p\}_{p=1\dots K}$ is shown in Fig. 4(b). The overall LRRS algorithm is shown in Algorithm 1.

Algorithm 1 The LRRS algorithm

Input: Regions set $\{R_p\}_{p=1\dots Z}$.

Initialization: $\{N_p\}_{p=1\dots K} = \emptyset$; Calculate mean intensity $\{q_p\}_{p=1\dots Z}$.

Forming new regions set $\{R'_p\}_{p=1\dots Z}$ using global thresholding.

for each region R'_p **do**

if $A(R'_p) > T_{area}$ and $V > 2$ **then**

repeat

 Local threshold in R'_p based on the mean intensity in R'_p .

 Update current R'_p with the local threshold results.

until $A(R'_p) \leq T_{area}$ or $V \leq 2$

else

 Assign current region to the Candidate regions set, $R'_p \rightarrow \{N_p\}_{p=1\dots K}$.

end if

end for

Output: Candidate regions set $\{N_p\}_{p=1\dots K}$.

C. Local Double Ellipse Descriptor Analysis

In this section, a novel descriptor, LDED, which is based on a double ellipsoidal model, is proposed. The LDED utilizes the candidate regions $\{N_p\}_{p=1\dots K}$ and its surrounding local features to discriminate the melanocytes and other cytological components. The details of the LDED analysis are presented in the following subsections.

1) *Construction of the Elliptical Model:* At first, an ellipse is fitted based on the boundary points of a candidate region N_p using the direct least-squares fitting algorithm [20] (see the

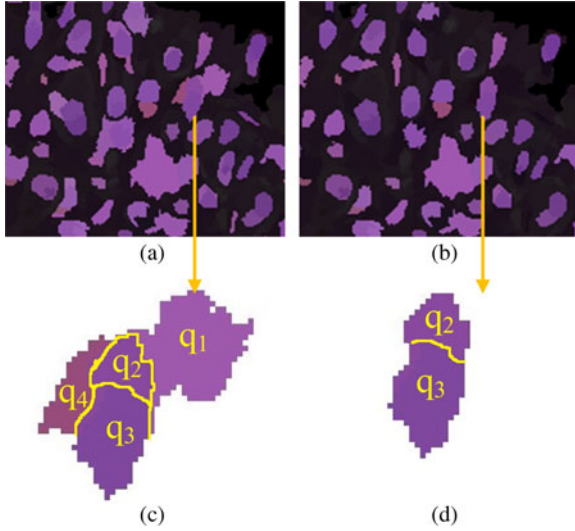


Fig. 4. The output of the local region recursive segmentation. (a) Image obtained by applying step 1 on Fig. 3(b). (b) Image obtained by applying step 2 on (a). (c) and (d) are magnified image of a local region in (a) and (b), respectively. q_p is the mean intensity of region p .

Appendix). Fig. 5(a) shows the ellipses obtained by fitting the boundary points of the image shown in Fig 4(b). It is observed in Fig. 5(a) that most of the nuclei are fitted well with ellipses. However, there are a few regions (for example, the regions labeled as A , B , and C in the figure) that have irregular shapes and cannot be fitted well by an ellipse. These regions need to be eliminated for efficient nuclei detection.

2) *Construction of the Double Ellipse Descriptor*: Note that using the aforementioned elliptical model, we can measure the shape of the nuclei region. However, in order to capture the local information of the nuclei region, we need to build another elliptical model that have larger capturing range. Let E_{IN} denote the earlier mentioned elliptical model, and henceforth referred to as the inner elliptical model. We now build another elliptical model E_{OT} , named outer/enlarged elliptical model, such that it has the same centroid position with that of E_{IN} , but has larger minor and major axes. The outer elliptical model is proposed to capture the surrounding local information of the current candidate nuclei region. Typically, the enlarged major and minor axes have a factor of 1.4 (the enlargement factor decides the local range of the measurement). Fig. 5(c) shows the formation of outer elliptical model around the inner elliptical model for each nucleus region N_p . Denote the points set inside the inner elliptical model as Q_{IN} , the points set inside the outer elliptical model as Q_{OT} , and the points set between the inner and outer elliptical model as Q_{IO} , i.e., $Q_{IO} = Q_{OT} - Q_{IN}$. The Q_{IN} , Q_{IO} , and Q_{OT} constitute the LDED as shown in Fig. 5(b). The Q_{IN} is shown in Fig. 5(b) as the white area, Q_{IO} is the shadow area between E_{IN} and E_{OT} , and Q_{OT} is the area consisting of Q_{IN} and Q_{IO} . The Q_{IO} can measure the surrounding area of the candidate nuclei. Based on the defined LDED, we now discuss two measurements in the following.

3) *Detection of the Nuclei Using Ellipticity Parameter*: As shown in Fig. 5(a), a few false positives, i.e., the regions which

are not true nuclei, are expected to be present in the candidate regions $\{N_p\}_{p=1...K}$. Based on the assumption that a nuclei typically has an elliptical shape, we can filter out the false positives by using the ellipticity of a region with the inner elliptical model. It is possible to detect the false positives by thresholding $\|\mathbf{D}\hat{\mathbf{a}}\|^2$ obtained using (27) (see the Appendix). However, in this paper, we propose to use another measure, which is visually more intuitive to detect the false positives. Denote S as the set of pixels in a candidate region N_p . A parameter which measures the ellipticity e_E is defined as follows:

$$e_E \equiv 1 - \frac{|S \oplus Q_{IN}|}{|Q_{IN}|} = \frac{|S \cap Q_{IN}|}{|Q_{IN}|} \quad (5)$$

where \oplus is the exclusive OR operation, and $|\cdot|$ is the cardinality of a point set. Note that a region with a high-ellipticity parameter e_E will have a closer match to an the elliptical shape, and is likely to be a nucleus. On the other hand, a region with a low-ellipticity parameter e_E indicates that this region contains noisy connecting component (either concave or convex component), and is not likely to be a true nucleus region.

Three examples with different ellipticity parameters e_E are shown in the first two columns of Fig. 6. In Fig. 6(b), (f), and (j), the candidate regions are represented by white pixels. The ellipse represents the inner elliptical model E_{IN} . The e_E value indicates the corresponding ellipticity parameters. Note that the candidate regions shown in Fig. 6(b) and (f) are true nuclei regions with high values of e_E ($e_E = 0.90$ and $e_E = 0.94$, respectively). In contrast, the candidate region shown in Fig. 6(j) is a false nuclei region with a low value of e_E ($e_E = 0.65$). In other words, using this parameter, we can eliminate the false nuclei regions. A segmented region N_p corresponds to a nucleus if the following condition is satisfied:

$$e_E^{N_p} \geq \tau_E \quad (6)$$

where $e_E^{N_p}$ is the ellipticity parameter for region N_p calculated using (5), and τ_E is a preselected threshold. Let us assume that the aforementioned test is satisfied by K' regions, i.e., there are K' nuclei in the image. Let these regions be denoted by $\{N'_p\}_{p=1...K'}$.

4) *Detection of the Melanocytes*: After the nuclei detection, the task is now to distinguish the melanocytes from other keratinocytes. Note that in the epidermis skin image, a normal melanocyte is typically a small cell with a dark nuclei, lying singly in the basal of epidermis. In digitized image, it appears to lie in a clear space and retracted from other cells, due to the shrinkage of cytoplasm [21]. As for the atypical melanocytes, the nuclei becomes larger and has irregular contour, but the pattern is the same. This pattern can be easily observed in Fig. 7(a) and (b). Note that we focus on the red channel of the RGB color image for LDED analysis in this paper. It is observed that the nuclei of the melanocytes prefer to have low intensity value, while its spatial surrounding space presents higher intensity value. It is shown in the histogram that there are two distinct modes present. The centers of these two modes lie around intensity value 110 and 175. On the other hand, in the case of other keratinocytes [shown in Fig. 7(c) and (d)], it is difficult to find the two distinct modes and the histogram usually is unimodal.

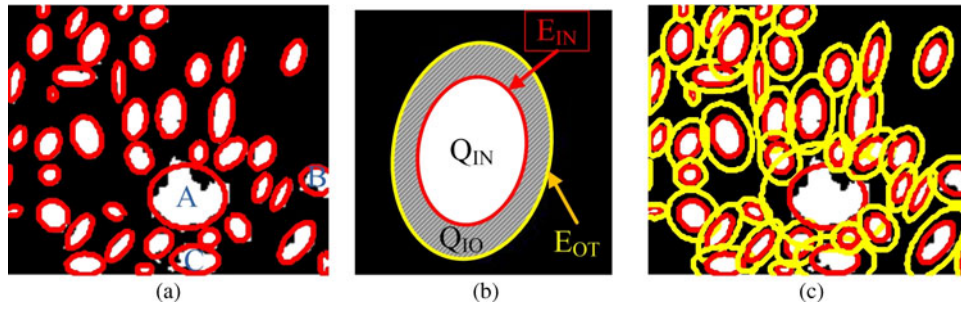


Fig. 5. Elliptical modeling for each nucleus. (a) Original single elliptical model on Fig. 4(b). (b) Illustration of the LDED. (c) Double elliptical model on Fig. 4(b).

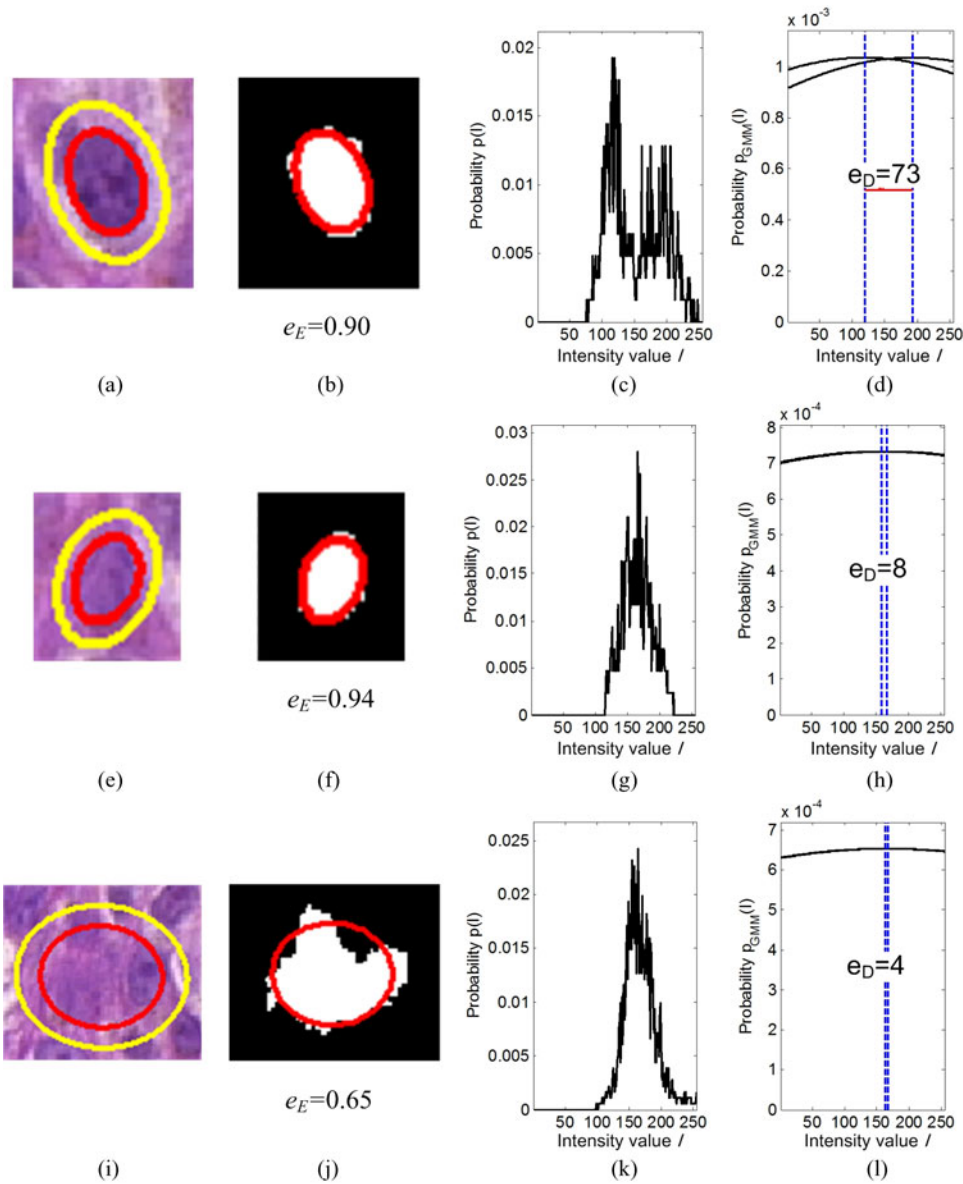


Fig. 6. Illustrations of two parameters e_E and e_D for three different candidate nuclei regions. (a), (e), and (i) Three candidate nuclei regions with their corresponding LDED overlapped. (b), (f), and (j) Ellipticity parameters provided by the inner elliptical model E_{IN} . (c), (g), and (k) Pdf of the intensity values set obtained by the outer elliptical model E_{OT} . We used the red channel intensity from the color RGB image in this paper. (d), (h), and (l) Correspondence GMM estimated from (c), (g), and (k), respectively. The Gaussian model is represented by the solid black line and the center of each Gaussian model is indicated by the dashed line. The parameter e_D for these three cases are 73, 8, and 4, respectively. Note that the first row shows a case of melanocyte, the second row shows a case of other keratinocytes, the third row shows a case of noisy component which is not a nucleus.

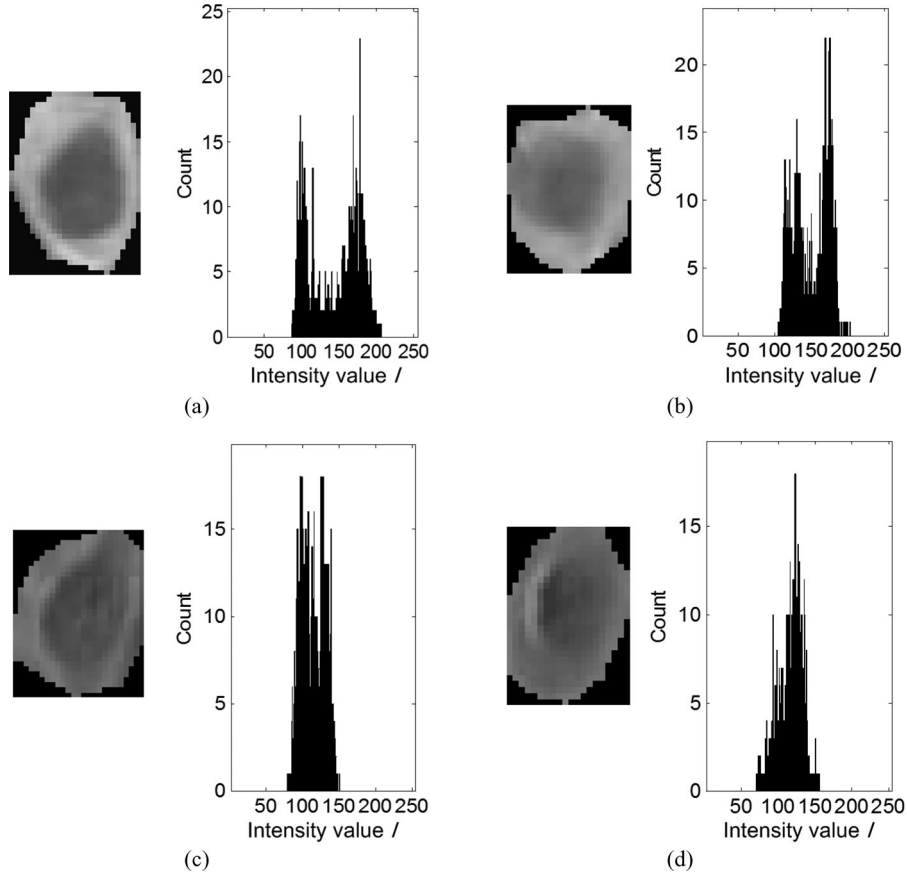


Fig. 7. Manually cropped melanocytes and other keratinocytes as well as the corresponding histograms. (a) and (b) Two typical melanocytes. (c) and (d) Two other keratinocytes. Note that the images are obtained from the red channel of the color image. The horizontal axis is the gray value, whereas the vertical axis is the counting number of corresponding intensity value in red channel.

Based on the histogram patterns shown in Fig. 7, we propose a novel method to distinguish the melanocytes and other keratinocytes. The basic idea is that we first model the underlying probability density function pdf as a two univariate Gaussian mixture model (GMM). The distance of the two Gaussian modes is then used to distinguish the melanocytes and other keratinocytes.

Denote the pixel intensity set inside the outer elliptical model E_{OT} for the candidate nuclei region N_p as I^{N_p} . Let the means and covariances of this two Gaussian mixture model be denoted as μ_i and σ_i^2 ($i = 1, 2$), respectively. Denote I as an observed sample, which is a pixel intensity value observed from the intensity set I^{N_p} . The pdf of the intensity value is expressed as follows:

$$p(I|\theta) = \sum_{i=1}^2 P(\omega_i) p(I|\omega_i, \theta_i) \quad (7)$$

where θ represents the set of four unknown parameters $(\mu_1, \mu_2, \sigma_1^2, \sigma_2^2)$. The two modes, denoted by classes ω_1 and ω_2 , indicate the Gaussian distribution corresponding to the current observed sample I . $P(\omega_i)$ is the *prior probability* for the two Gaussian modes in the GMM, and $p(I|\omega_i, \theta_i)$ is the class *conditional probability* which follows the Gaussian distribution

as follows:

$$p(I|\omega_i, \theta_i) = \frac{1}{\sqrt{2\pi\sigma^2}} \exp\left(-\frac{(I - \mu_i)^2}{2\sigma^2}\right). \quad (8)$$

In order to estimate the parameters set θ , we evaluate the log likelihood of the observed intensity values in the intensity set I^{N_p} as follows:

$$L(\theta) = \log \prod_{j=1}^n p(I_j|\theta) = \sum_{j=1}^n \log \left[\sum_{i=1}^2 P(\omega_i) p(I_j|\omega_i, \theta_i) \right] \quad (9)$$

where n is the total number of intensity values in the intensity set I^{N_p} and I_j is the j th intensity value. Note that finding the maximum likelihood with respect to the parameters θ using (9) is difficult as we cannot find a closed-form solution for it. The parametric expectation maximization (EM) algorithm is used to estimate the parameter. In EM algorithm, a modified log likelihood function $\tilde{L}(\theta)$ is calculated by introducing the *a posteriori* $P(\omega_i|I_j, \theta_i)$ as follows:

$$\tilde{L}(\theta) = \sum_{j=1}^n \sum_{i=1}^2 P(\omega_i|I_j, \theta_i) \log P(\omega_i) p(I_j|\omega_i, \theta_i). \quad (10)$$

The objective now is to find the parameter set θ that will maximize $\tilde{L}(\theta)$. In EM algorithm, this is done iteratively where

each iteration consists of two steps: expectation (E) step and maximization (M) step. In the E-step, *a posteriori* probability is estimated using the Bayes rule with a given parameter set θ as follows:

$$P(\omega_i|I_j, \theta_i) = \frac{P(\omega_i)p(I_j|\omega_i, \theta_i)}{\sum_{k=1}^2 P(\omega_k)p(I_j|\omega_k, \theta_k)}. \quad (11)$$

In the M-step, the parameters that maximize the log likelihood function in (10) are estimated as follows:

$$\mu_i = \frac{\sum_{j=1}^n P(\omega_i|I_j, \theta_i)I_j}{\sum_{j=1}^n P(\omega_i|I_j, \theta_i)} \quad (12)$$

$$\sigma_i^2 = \frac{\sum_{j=1}^n P(\omega_i|I_j, \theta_i)(I_j - \mu_i)^2}{\sum_{j=1}^n P(\omega_i|I_j, \theta_i)} \quad (13)$$

$$P(\omega_i) = \frac{1}{n} \sum_{j=1}^n P(\omega_i|I_j, \theta_i). \quad (14)$$

The EM algorithm recursively repeats the expectation and the maximization steps until $\tilde{L}(\theta)$ converges [22]. The estimated GMM represents the underlying pdf of the intensity values retrieved by the outer elliptical model. Based on the estimated GMM, the following parameter is proposed to distinguish the melanocytes and other keratinocytes:

$$e_D = |\mu_1 - \mu_2|. \quad (15)$$

Note that the parameter e_D computes the mean difference of the estimated GMM. Intuitively, if the underlying distribution of the I^{N_p} is a distinct bimodal distribution, the parameter e_D has a large value. On the other hand, if the underlying distribution of the I^{N_p} is a unimodal distribution, the parameter e_D has a small value. Basically, this parameter measures the local intensity features of the nuclei regions and will serve as an important factor in identifying the melanocytes from other candidate regions. Three examples of computing the parameter e_D are shown in the Fig. 6. Three candidate nuclei regions with the overlapped LDEDs are shown in Fig. 6(a), (e), and (i). The corresponding pdfs of the intensity sets obtained by the outer elliptical model E_{OT} are shown in Fig. 6(c), (g), and (k), respectively. The corresponding GMM estimated using the EM algorithm are shown in Fig. 6(d), (h), and (l), respectively. It is observed that for the true melanocyte (shown in the first row), the two estimated Gaussian modes are distinctly apart from each other, and result in a high value of e_D ($e_D = 73$). For the nonmelanocytes regions (shown in the second and third rows of Fig. 6), the modes in the GMM overlap, and we obtain a low value of e_D ($e_D = 8$ and $e_D = 4$ as shown in Fig. 6(h) and (l), respectively).

Using the parameter e_D measured by the LDED, we can now detect the melanocytes from the candidate nuclei regions $\{N'_p\}_{p=1...K'}$. A segmented region N'_p corresponds to a melanocyte if the following condition is satisfied:

$$e_D^{N'_p} \geq \tau_D \quad (16)$$

where $e_D^{N'_p}$ is the parameter of region N'_p calculated using (15), and τ_D is the threshold for e_D .

Algorithm 2 The algorithm for LDED analysis

Input: Candidate nuclei regions set $\{N_p\}_{p=1...K}$.

Initialization: $\{M_p\}_{p=1...O} = \emptyset$.

for each region N_p **do**

 Construct double elliptical model.

 Calculate parameter e_E using Eq. 5.

 Calculate parameter e_D using Eq. 12 and Eq. 15 via EM algorithm.

if $e_D^{N_p} \geq \tau_D$ and $e_E^{N_p} \geq \tau_E$, **then**

 Assign current region to the melanocyte regions set,

$N_p \rightarrow \{M_p\}_{p=1...O}$.

end if

end for

Output: Melanocyte regions set $\{M_p\}_{p=1...O}$.

Note that the ellipticity parameter e_E serves as an indicator of the nuclei region, while the second parameter e_D serves as an indicator for the melanocytes. From experiments, it has been found that $\tau_E \approx 0.8$ and $\tau_D \approx 34$ provides good performance. The algorithm for the LDED analysis is shown in Algorithm 2. An illustration of the LDED analysis is shown in Fig. 8. The original image is shown in Fig. 8(a), whereas the formation of the LDED is shown in Fig. 8(b). Fig. 8(c) illustrates the LDED superimposed on the original image, and the two parameters are measured. The final melanocytes detection result is shown in Fig. 8(d). It is observed that the technique could find all the melanocytes in the image.

III. PERFORMANCE EVALUATION

We have evaluated the proposed technique on 30 different skin histopathology images of epidermis. These images are captured from different skin tissue samples corresponding to normal skin, nevus, and melanoma. These images are captured on Carl Zeiss MIRAX MIDI Scanning system [23].

For the performance evaluation, the melanocytes manually identified are treated as the ground truths. We define N_{GT} as the total number of ground truths, N_{DO} as the total number of detected objects, N_{TP} as the number of true positives (i.e., correctly detected objects), N_{FP} as the number of false positives (i.e., falsely detected objects). The positive prediction rate (PPR) and the sensitivity (SEN) are defined as follows:

$$PPR = \frac{N_{TP}}{N_{DO}} \times 100\% \quad (17)$$

$$SEN = \frac{N_{TP}}{N_{GT}} \times 100\%. \quad (18)$$

A. Quantitative Evaluation

In this section, we present the quantitative evaluation of the proposed technique. In order to calculate the parameter τ_E and τ_D for the proposed technique, two of the images are selected. In these two images, 50 melanocytes are manually labeled, and the value of e_E and e_D for each melanocyte is calculated. We

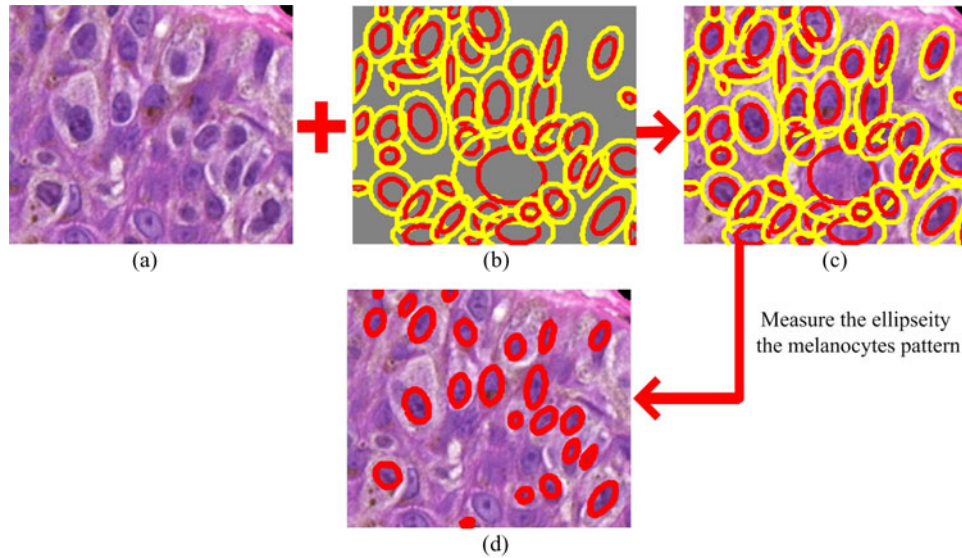


Fig. 8. Illustration of the LDED analysis. (a) Original image. (b) All the LDEDs. (c) LDEDs overlap onto the original image to perform the analysis. (d) Detection of the melanocytes using the analysis on two parameters e_E and e_D . The detected melanocytes are label as red ellipses.

TABLE I
PERFORMANCE OF THE PROPOSED TECHNIQUE ON THE 28 TEST IMAGES

Index	Image Property		20× Magnification		30× Magnification		40× Magnification	
	μ	σ	PPR (%)	SEN (%)	PPR (%)	SEN (%)	PPR (%)	SEN (%)
1	135.54	31.95	72.09	83.78	75.57	85.68	80.00	86.49
2	170.04	24.24	62.78	84.47	64.94	86.24	68.14	94.07
3	116.16	41.92	73.91	80.95	71.43	95.24	83.33	95.24
4	118.43	30.34	76.32	87.81	77.19	88.28	78.81	91.18
5	130.27	22.72	77.81	84.32	80.39	83.43	84.67	89.54
6	142.51	28.36	75.00	78.57	67.83	78.57	75.56	71.43
7	179.91	25.78	78.71	70.59	84.62	64.71	83.33	88.24
8	146.57	35.35	65.79	89.29	66.67	85.71	75.86	88.57
9	141.65	32.31	72.55	82.22	73.79	82.22	80.95	82.22
10	141.06	34.08	63.55	90.67	58.93	88.00	68.89	84.64
11	173.44	38.35	73.86	73.63	78.03	70.69	82.73	76.67
12	161.42	29.77	63.89	78.83	66.57	79.71	75.00	73.18
13	106.64	30.01	71.33	82.78	76.04	89.93	78.75	84.62
14	116.89	25.97	79.96	81.96	78.77	87.62	76.19	96.00
15	103.04	28.97	76.84	92.17	77.02	93.98	80.00	100.00
16	134.65	32.01	76.87	87.62	79.14	87.62	85.73	96.67
17	126.97	29.12	73.83	84.45	77.79	85.39	75.57	85.11
18	138.00	31.14	70.95	79.10	75.99	77.32	76.12	68.92
19	133.43	34.44	77.94	86.57	82.14	86.57	83.33	90.91
20	132.26	26.44	71.78	92.39	74.44	91.06	80.00	94.12
21	146.38	26.21	73.77	75.70	73.21	74.23	79.68	77.78
22	153.45	22.03	67.08	80.04	72.64	80.48	77.27	81.25
23	167.64	25.12	71.87	74.20	70.58	77.78	72.41	65.63
24	124.13	28.86	80.77	89.42	78.88	92.25	81.58	96.88
25	137.64	25.23	80.92	90.05	82.50	90.95	85.00	87.93
26	125.89	27.34	71.82	87.56	75.75	87.56	80.77	87.50
27	104.82	33.39	83.72	67.92	72.41	79.25	81.36	90.57
28	101.83	33.49	83.68	84.34	79.52	87.95	84.04	92.77
Average	136.10	29.82	73.91	82.91	74.74	84.23	79.11	86.36

then performed the trail-and-error test, the parameter τ_E and τ_D which achieved the best PPR and SEN are selected as the parameter τ_E and τ_D for the proposed technique (specifically, $\tau_E = 0.8$ and $\tau_D = 34$). These two parameters are then used for the performance evaluation on the remaining 28 test images with changes on zoom factor. The evaluation result is shown in Table I. In Table I, the image index is shown in the first column. In the second and third columns, the image properties

(i.e., the mean intensity μ and the standard variance σ) of red channel image are presented. The remaining columns show the performance of the proposed technique, in terms of PPR and SEN, on different magnification level (20×, 30×, and 40×). The average performance is shown in the last row of Table I. It is observed that the proposed technique provides a robust performance on these 28 test images with different intensity and zooming levels.

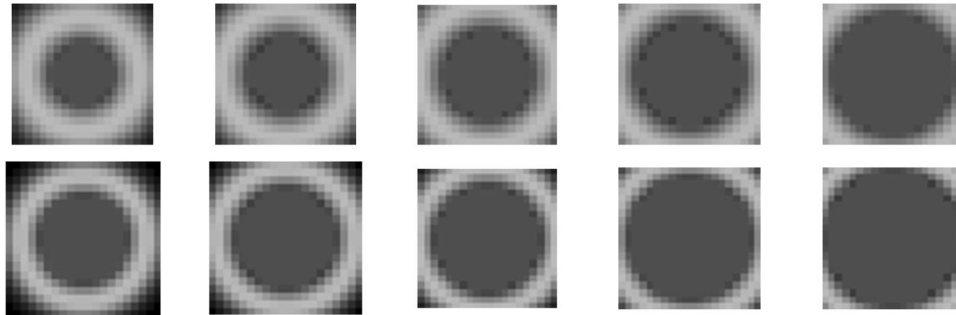


Fig. 9. Ten templates with size 20×20 used in the TM techniques. Note the variation of the center heart radii and the ring thickness. The templates are magnified for demonstration purpose.

B. Comparison With TM Technique

Since this is the first technique to solve the melanocytes segmentation problem, there is no other equivalent technique in the literature that can be compared with the proposed technique. Therefore, we compare the proposed technique with a possible alternative technique, known as TM. Note that the TM is a widely used technique for pattern detection in medical imaging [13], [24]. A set of 30 templates is designed to capture the “MPattern” and selected 10 templates are shown in Fig. 9. The templates are designed according to 30 manually selected melanocytes. Note that we designed 30 templates with different sizes in terms of the template size (15×15 , 20×20 , and 25×25 pixels), center heart radii (8, 9, 10, 11, and 12 pixels), and the ring thickness (2 and 3 pixels), in order to create the variations. The intensity for the heart of the template and the ring of the template are assigned according to the mean value of the corresponding regions in the 30 samples of manually selected melanocytes [two examples are shown in Fig. 7(a) and (b)]. In the TM implementation, each template is first applied on the image by using the normalized cross correlation (NCC) [25]. Denote the NCC output of the i th template as O_i , and the 2-D coordinate in the image as (u, v) . The candidate pixel $J_i(u, v)$ obtained from the i th template is as follows:

$$J_i(u, v) = \begin{cases} J_i(u, v) & \text{if } O_i(u, v) \geq \tau_{TM} \\ 0 & \text{otherwise} \end{cases} \quad (19)$$

where T_{TM} is a threshold for each output. The τ_{TM} is set to 0.85 since it provides the best performance. The accumulated map O_{acc} for all 30 templates are calculated as follows:

$$O_{acc} = \sum_{i=1}^{30} \sum_{(u,v) \in \Omega} J_i(u, v) \quad (20)$$

where Ω represents the image domain. The final result is a binary image which is determined using a threshold of 2 on O_{acc} .

The comparison of the proposed technique and the TM technique is performed on the images with $30\times$ magnification. We denote the first step of the proposed technique as ML which consists of the mean-shift segmentation as the initial segmentation and the proposed LRRS algorithm. We denote the overall proposed technique as ML+LDED, where the LDED analysis is performed based on the output of the ML. The performance of the ML and ML+LDED is shown in Table II.

TABLE II
PERFORMANCE OF THE PROPOSED TECHNIQUE (ML AND ML+LDED) AND TM TECHNIQUE ON THE TEST IMAGES (WITH $30\times$ MAGNIFICATION)

Technique	PPR (%)	SEN (%)
ML	43.22	97.24
ML+LDED	74.74	84.23
TM	21.53	65.83

It is shown in Table II that by using the ML, almost all the ground truth melanocytes are segmented with the SEN at 97.24%. However, using ML alone cannot differentiate the melanocytes and other keratinocytes, which leads to a low PPR of 43.22%. In other words, a large number of nonmelanocyte regions are included. After performing the LDED analysis, most of the false positives are filtered out which results in a higher PPR (about 74.74%), while still providing satisfactory SEN (84.23%). As for the TM technique, the low PPR (21.53%) indicates that the TM technique does not have the ability to distinguish the melanocytes and other keratinocytes. Also, the TM technique provides a low SEN (65.83%) because it cannot capture the variations of the melanocytes in the epidermis.

For the visual comparison, three close-up examples cropped from the test images are shown in Fig. 10. These images are captured from different skin tissues, and parameters $\tau_E = 0.8$ and $\tau_D = 34$ were used for the detection. Note that Fig. 10(a), (f), and (k) show three original color histopathological images. Fig. 10(b), (g), and (l) show the corresponding ground truth. The melanocytes are indicated by stars. The last three columns show the results obtained using the ML, ML+LDED, and TM technique, respectively. The detected regions are presented as the thick contours. It is observed that the results provided by the ML technique [shown in Fig. 10(c), (h), and (m)] include almost all the melanocytes and other keratinocytes. In comparison, the ML+LDED is able to filter out nonmelanocytes regions [shown in Fig. 10(d), (i), and (n)] very effectively, and the false detection rate is very low. In Fig. 10(i), there are two false positives (indicated by hollow arrows). That is because the candidate nuclei regions are very close to typical melanocytes where its surrounding cytoplasm are retracted. As for the TM technique, a large number of patterns have been detected as melanocytes since there are many cytological components similar to that of the melanocyte patterns [shown in Fig. 10(e), (j), and (o)]. In Fig. 10(j), the TM technique misses most of the ground

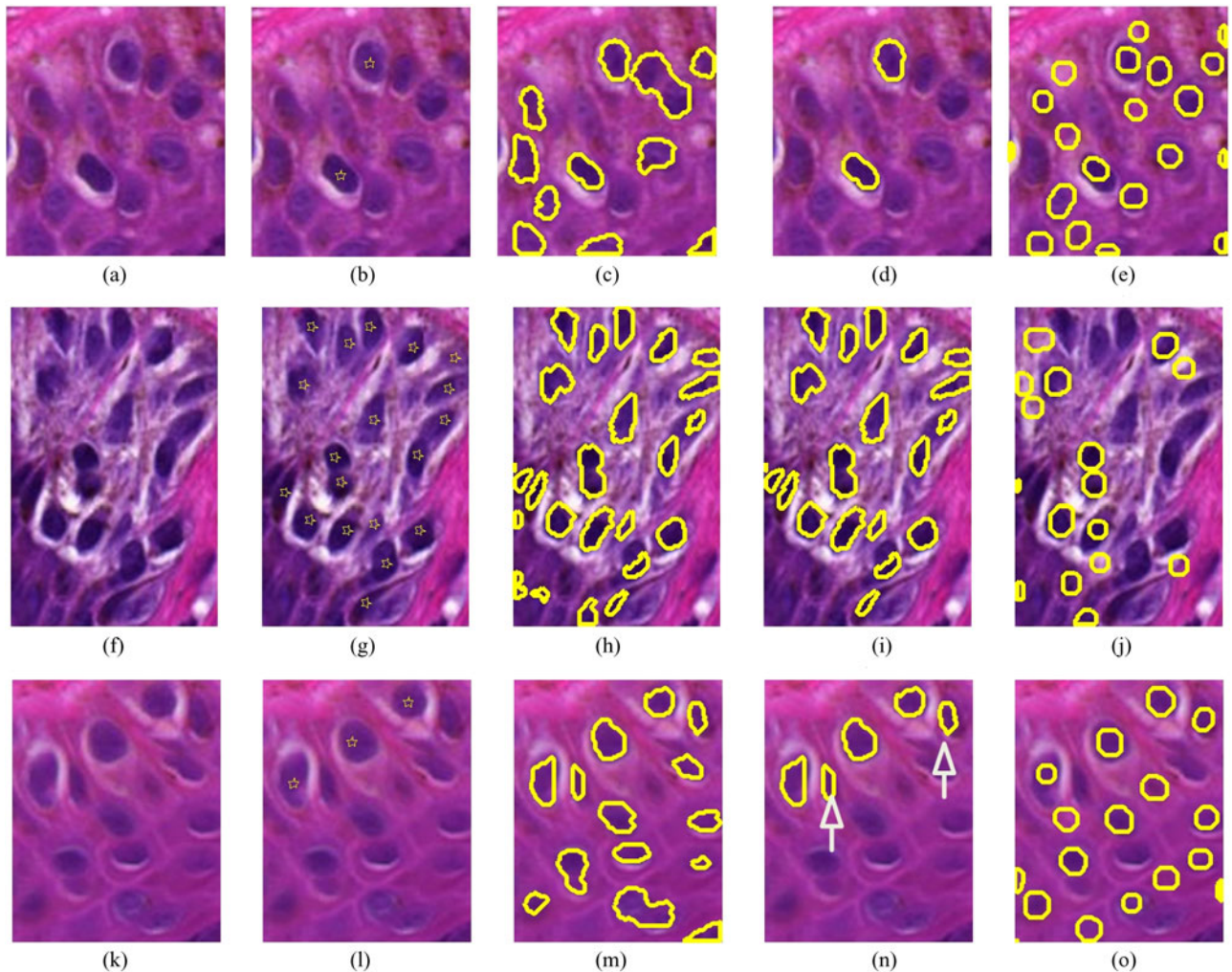


Fig. 10. Three examples for qualitative evaluation. (a), (f), and (k) Three original color histopathological images. (b), (g), and (l) The ground truths indicated by stars. (c), (h), and (m) Result provided by ML. (d), (i), and (n) Result provided by ML+LDED. (e), (j), and (o) The result provided by TM. Note that detected regions are presented as the thick contours.

truths because it is very difficult to model a good template set that can capture the size and shape variations of the natural melanocytes. Overall, the proposed technique is able to provide a good performance in the test images set.

All experiments were carried out on a 2.4-GHz Intel Core II Duo CPU with 3-GB RAM using MATLAB 7.04. On average, the proposed technique takes 6 s to segment the melanocytes from a 512×512 pixels RGB color image. On the other hand, the TM technique takes 3 s to detect the melanocytes in the image.

IV. CONCLUSIONS

This paper presents a simple but effective computer-aided technique for segmentation of the melanocytes in the skin histopathological image. The candidate nuclei regions are first extracted through the mean shift, and the proposed local region recursive segmentation algorithm. The local double ellipse descriptor then incorporates the biological feature of melanocytes and provides robust parameters to identify the melanocytes. The evaluation using 30 histopathological images with differ-

ent zooming factors shows that the proposed technique is able to segment the melanocytes with over 80% sensitivity rate and over 70% positive prediction rate. In future, we have planned to analyze the cytological and architectural features of the detected melanocytes in order to grade and diagnose the skin tissues.

APPENDIX

In Section III(c), the elliptical model was introduced. In this appendix, the direct least-square fitting algorithm is explained for fitting an ellipse with a nucleus.

Let (u, v) be a 2-D point of an ellipse, and the ellipse is modeled using the following implicit second-order polynomial:

$$E(u, v) = au^2 + b^2 + cv^2 + du + ev + f = 0 \quad (21)$$

with an ellipse-specific constraint $b^2 - 4ac < 0$, where a, b, c, d, e , and f denote the ellipse coefficients. Equation (21) can be rewritten in the vector form as follows:

$$E(u, v) = \mathbf{a}\mathbf{u} = 0 \quad (22)$$

where $\mathbf{a} = [a, b, c, d, e, f]^T$ and $\mathbf{u} = [u^2, uv, v^2, u, v, 1]$.

Assuming that $b^2 - 4ac = -r$, the inequality constraint $b^2 - 4ac < 0$ can be converted into an equality constraint $4ac - b^2 = r$ [20], where r is an arbitrary positive number. Without any loss of generality, let $r = 1$. The equality constraint can then be represented in matrix form as follows:

$$\mathbf{a}^T \mathbf{C} \mathbf{a} = 1 \quad (23)$$

where

$$\mathbf{C} = \begin{bmatrix} 0 & 0 & 2 & 0 & 0 & 0 \\ 0 & -1 & 0 & 0 & 0 & 0 \\ 2 & 0 & 0 & 0 & 0 & 0 \\ 0 & 0 & 0 & 0 & 0 & 0 \\ 0 & 0 & 0 & 0 & 0 & 0 \\ 0 & 0 & 0 & 0 & 0 & 0 \end{bmatrix}. \quad (24)$$

Assume a set of B boundary points corresponding to a candidate region. In the ideal case, all the boundary points will be on an ellipse defined by \mathbf{a} , and will satisfy the following equation:

$$\|\mathbf{D} \mathbf{a}\|^2 = 0 \quad (25)$$

where the design matrix \mathbf{D} is defined as follows:

$$\mathbf{D} = \begin{bmatrix} u_1^2 & u_1 v_1 & v_1^2 & u_1 & v_1 & 1 \\ \vdots & \vdots & \vdots & \vdots & \vdots & \vdots \\ u_i^2 & u_i v_i & v_i^2 & u_i & v_i & 1 \\ \vdots & \vdots & \vdots & \vdots & \vdots & \vdots \\ u_B^2 & u_B v_B & v_B^2 & u_B & v_B & 1 \end{bmatrix} \quad (26)$$

where (u_i, v_i) denote the 2-D coordinate of the i th boundary point for the region. In general, the boundary points will not form a perfect ellipse and (25) will not be satisfied. The optimal coefficients vector $\hat{\mathbf{a}}$ corresponding to the best matched ellipse can be estimated by solving the following least-squares minimization:

$$\hat{\mathbf{a}} = \arg \min_{\mathbf{a}} \|\mathbf{D} \mathbf{a}\|^2 \text{ subject to } \mathbf{a}^T \mathbf{C} \mathbf{a} = 1. \quad (27)$$

Equation (27) can be solved via a Lagrange multiplier method [20].

ACKNOWLEDGMENT

The authors would like to thank the anonymous reviewers for the comments that helped to improve the quality of this paper.

REFERENCES

[1] I. Maglogiannis and C. Doukas, "Overview of advanced computer vision systems for skin lesions characterization," *IEEE Trans. Inf. Technol. Biomed.*, vol. 13, no. 5, pp. 721–733, Sep. 2009.
 [2] A. C. Society, "What are the key statistics about melanoma?" Amer. Cancer Soc., Tech. Rep., 2008.
 [3] D. Rigel, J. Russak, and R. Friedman, "The evolution of melanoma diagnosis: 25 years beyond the ABCDs," *CA: Canc. J. Clinic.*, vol. 60, no. 5, pp. 301–316, 2010.
 [4] J. Pawley, *Handbook of Biological Confocal Microscopy*. New York: Springer-Verlag, 2006.
 [5] V. Kumar, A. Abbas, and N. Fausto, *Robbins and Cotran Pathologic Basis of Disease*. Amsterdam, The Netherlands/Philadelphia, PA: Elsevier/Saunders, 2005.
 [6] S. Ismail, A. Colclough, J. Dinnen, D. Eakins, D. Evans, E. Gradwell, J. O'Sullivan, J. Summerell, and R. Newcombe, "Observer variation in

histopathological diagnosis and grading of cervical intraepithelial neoplasia," *Brit. Med. J.*, vol. 298, no. 6675, p. 707, 1989.
 [7] M. Gurcan, T. Pan, H. Shimada, and J. Saltz, "Image analysis for neuroblastoma classification: Segmentation of cell nuclei," in *Proc. 28th IEEE Annu. Int. Conf. EMBS*, 2006, pp. 4844–4847.
 [8] S. Petushi, F. U. Garcia, M. M. Haber, C. Katsinis, and A. Tozeren, "Large-scale computations on histology images reveal grade-differentiating parameters for breast cancer," *BMC Med. Imag.*, vol. 6, p. 14, 2006.
 [9] L. Coelho, A. Shariff, and R. Murphy, "Nuclear segmentation in microscope cell images: A hand-segmented dataset and comparison of algorithms," in *Proc. IEEE Int. Symp. Biomed. Imag.: Nano Macro*, 2009, pp. 518–521.
 [10] L. E. Boucheron, "Object- and spatial-level quantitative analysis of multi-spectral histopathology images for detection and characterization of cancer," Ph.D. dissertation, Univ. California, Santa Barbara, Mar. 2008.
 [11] X. Chen, X. Zhou, and S. Wong, "Automated segmentation, classification, and tracking of cancer cell nuclei in time-lapse microscopy," *IEEE Trans. Biomed. Eng.*, vol. 53, no. 4, pp. 762–766, Apr. 2006.
 [12] T. Nattkemper, H. Ritter, and W. Schubert, "A neural classifier enabling high-throughput topological analysis of lymphocytes in tissue sections," *IEEE Trans. Inf. Technol. Biomed.*, vol. 5, no. 2, pp. 138–149, Jun. 2001.
 [13] S. Naik, S. Doyle, S. Agner, A. Madabhushi, M. Feldman, and J. Tomaszewski, "Automated gland and nuclei segmentation for grading of prostate and breast cancer histopathology," in *Proc. 5th IEEE Int. Symp. Biomed. Imag.: Nano Macro ISBI 2008*, pp. 284–287.
 [14] O. Sertel, U. Catalyurek, H. Shimada, and M. Guican, "Computer-aided Prognosis of Neuroblastoma: Detection of mitosis and karyorrhexis cells in digitized histological images," in *Proc. 31st IEEE Annu. Int. Conf. EMBS*, 2009, pp. 1433–1436.
 [15] A. N. Basavanthally, S. Ganesan, S. Agner, J. P. Monaco, M. D. Feldman, J. E. Tomaszewski, G. Bhanot, and A. Madabhushi, "Computerized image-based detection and grading of lymphocytic infiltration in HER2+ breast cancer histopathology," *IEEE Trans. Biomed. Eng.*, vol. 57, no. 3, pp. 642–653, Mar. 2010.
 [16] V. Korde, H. Bartels, J. Barton, and J. Ranger-Moore, "Automatic segmentation of cell nuclei in bladder and skin tissue for karyometric analysis," *Anal. Quant. Cytol. Histol.*, vol. 31, no. 2, p. 83, 2009.
 [17] D. Comaniciu and P. Meer, "Mean shift: A robust approach toward feature space analysis," *IEEE Trans. Pattern Anal. Mach. Intell.*, vol. 24, no. 5, pp. 603–619, May 2002.
 [18] J. Sethian, *Level Set Methods and Fast Marching Methods: Evolving Interfaces in Computational Geometry, Fluid Mechanics, Computer Vision, and Materials Science*. Cambridge, U.K.: Cambridge Univ. Press, 1999.
 [19] N. Otsu, "A threshold selection method from gray-level histograms," *IEEE Trans. Syst., Man, Cybern.*, vol. 9, no. 1, pp. 62–66, 1979.
 [20] M. Fitzgibbon, A. W. Pilu, and R. B. Fisher, "Direct least-squares fitting of ellipses," *IEEE Trans. Pattern Anal. Mach. Intell.*, vol. 21, no. 5, pp. 476–480, 1999.
 [21] D. Weedon and G. Strutton, *Skin Pathology*. vol. 430, New York: Churchill Livingstone, 2002.
 [22] C. Bishop, *Neural Networks for Pattern Recognition*. Oxford, U.K.: Oxford Univ. Press, 1995.
 [23] C. Z. M. GmbH. (2009). "Mirax MIDI—the versatile slide scanner for research and routine," [Online]. Available: www.zeiss.de/mirax.
 [24] I. Sintorn, M. Homman-Loudiyi, C. Söderberg-Nauclér, and G. Borgefors, "A refined circular template matching method for classification of human cytomegalovirus capsids in tem images," *Comput. Methods Programs Biomed.*, vol. 76, no. 2, pp. 95–102, 2004.
 [25] J. Lewis, "Fast normalized cross-correlation," in *Proc. Conf. Vision Interface*, 1995, vol. 10, pp. 120–123.



Cheng Lu received the B.Sc. and M.Sc. degrees in computer engineering from Information Engineering College, Northwest Agriculture and Forestry University, Shaanxi, China, in 2006 and 2008. He is currently working toward the Ph.D. degree in electrical engineering in the Multimedia Computing and Communication Lab, Department of Electrical Engineering, University of Alberta, Edmonton, AB, Canada from 2008 till now.

His research interest includes computer vision, medical image analysis, pattern recognition and super

per resolution imaging.

Mr. Lu is the recipient of the Chinese Scholarship Council scholarship for his Ph.D. studies.



Muhammad Mahmood received the medical degree from Aga Khan University, Medical College, Karachi, Pakistan. He did his anatomical pathology/clinical pathology residency Henry at Ford Hospital, Detroit, MI.

He is the recipient of an Advanced Selective Pathology Fellowship from Barnes-Jewish Hospital, Washington University Medical Center, Saint Louis, MO, and a Dermatopathology Fellowship from Ackerman Academy of Dermatopathology, New York, NY. For last six years, Dr. Mahmood is a practising

anatomical pathologist/dermatopathologist in Canada. He is currently with the Department of Lab Medicine and Pathology, University of Alberta Hospital, Edmonton, AB, Canada, and also with the Division of Anatomical Pathology, Walter Mackenzie Health Sciences Centre, Edmonton. His interests include melanocytic cutaneous lesions, cutaneous tumors and inflammatory dermatoses. He is also interested in developing postgraduate medical teaching for pathologists and dermatologists in training.

He is an American Board Certified Anatomical and Clinical Pathologist and American Board Certified Dermatopathologist.



Mrinal Mandal (M'99–SM'03) received the B.E. degree in electronics and communication engineering from the National Institute of Technology, Durgapur, India, and the M.A.Sc. and Ph.D. degrees in electrical and computer engineering from the University of Ottawa, Canada.

He is currently a Professor and Associate Chair in the Department of Electrical and Computer Engineering and is the Director of the Multimedia Computing and Communications Laboratory at the University of Alberta, Edmonton, AB, Canada. He was the recipient of Canadian Commonwealth Fellowship from 1993 to 1998, and Humboldt

Research Fellowship from 2005 to 2006 at Technical University of Berlin. He has been the Principal Investigator of projects funded by Canadian Networks of Centers of Excellence such as CITR and MICRONET, and is currently the Principal Investigator of a project funded by the Natural Sciences and Engineering Research Council, Moncton, Canada. He has published over 140 papers in refereed journals and conferences, and has a U.S. patent on lifting wavelet transform architecture. He has authored the book *Multimedia Signals and Systems* (Norwell, MA: Kluwer), and co-authored the book *Continuous and Discrete Time Signals and Systems* (Cambridge, U.K.: Cambridge Univ. Press). His current research interests include multimedia, image and video processing, multimedia communications, medical image analysis.



Naresh Jha received the Bachelor of Medicine and Bachelor of Surgery degrees from Delhi University, India, in 1979. He became a Fellow of the Royal College of Physicians of Canada in Radiation Oncology in 1987.

He has been a Senior Radiation Oncologist at the Cross Cancer Institute, University of Alberta, Edmonton, AB, Canada, since 1988. He specializes in head and neck, thyroid, and skin cancers. He participated in residency training in Radiation Oncology at the Cross Cancer Institute. He is a pioneer

of the submandibular salivary gland transfer—a ground-breaking technique to prevent radiation-induced xerostomia.